General comments

The authors would like to thank the two reviewers for their constructive comments that undoubtedly improved the quality of the manuscript. Both reviewers concisely summarised the key results of the study and highlighted the importance of the work to the ocean glider community. Both reviewers support/recommend publication.

Reviewer 1

Specific comments:

1) Energy flux error analysis using the regional Princeton Ocean Model (POM) configuration [paraphrased]. Our decision to use an idealised internal tide field rather than the POM simulation was driven by a desire to calculate a representative error for the method during a typical glider deployment over an ADCP, not the error specific to this mission. We feel that this is approach is more beneficial to the wider glider community than calculating a mission-specific error. A benefit of the idealised internal wave field approach is that it allows us to randomly change the relative phases of the baroclinic modes for each scenario and so that a wide range of phase space can be encapsulated by the Monte Carlo experiment without resorting to a large number of numerical model runs. The POM simulation was included to show that the observed internal tide energy flux and surface tidal ellipses were in agreement with previous studies – published direct observations are limited. However, due to the unusual stratification in the Wyville Thompson Basin and Faroe-Shetland Channel (namely a strong pycnocline at 500-600 m separating two low-buoyancy water masses), error calculated using the POM simulation would be too region-specific for wider use.

Minor comments:

1) Page 18. I feel that the description of the idealized internal tidal field should be moved into the main body of the text and not relegated to an Appendix. The authors have spent some time attempting to integrate the description of the idealised internal tide field into the main text, but felt that it disrupted the flow of the paper. The methodology is relatively long and the internal tide field description is a well-defined section that can easily be separated. However, the important detail that the relative phases of the baroclinic modes are randomly changed for each scenario has been highlighted by adding a sentence to the main text, '*A different random set of baroclinic mode phases is used for each scenario.*'.

2) Page 18, line 16. Do you really mean 'uniform stratification (N^2 = constant)'? Figure 7 suggests that this is not the case. Figure 7 is a uniform stratification case. The near-bottom intensification of energy flux is due to the superposition of baroclinic modes, rather than the effect of a deep pycnocline on baroclinic mode structure.

Reviewer 2

Specific points:

1) The only thing that I would recommend is using the existing model to assess some spatial decorrelation scale for internal tide amplitudes and energy at the mooring site. The authors describe that there may be considerable variability in space and they have a tool to calculate it. As is though, the manuscript is fine. Whether or not to do this, I leave to the authors. If we understand correctly, the suggestion is equivalent to asking: How close to the mooring site does the glider's target location have to be to ensure that measured density and measured velocity are correlated? This is indeed an good question and of interest when planning glider missions. However, in our experience, if environmental conditions allow a glider to hold station then it will be able to successfully center its dive cluster over the desired target location. It is therefore unlikely that a glider would achieve a tight dive cluster, but spatially separated from the mooring. This question will be considered in a future study when a longer co-located timeseries is available.

Minor points:

1) 1/16th wavelength diameter watch circle should be emphasized in figures and text because that appears to be relevant to these observations. 80 km tidal wavelength. 5 km watch circle. An additional Monte Carlo case has been included ($d/\lambda = 0.05$) that is a close match to estimates for the WTR. This new case is used to estimate the glider sampling error for the observations, instead of interpolating between the $d/\lambda = 0.03125$ and $d/\lambda = 0.0625$. This new case is highlighted in red in Figure 8 and in bold in Table 2.

2) Emphasize earlier on about the inability to separate S_2 and M_2. Maybe you want to call it D_2. The discussion of spring-neap in the summary is good. Maybe this could go in the intro. 40 h analysis window limits this further than the 3 day observation period implies. We now use the term D_2 where appropriate, and have included a new paragraph in Section 2 to explain D_2 the M_2-S_2 separation issue, '*As the glider was on-station for only 40 hours, the co-located timeseries is not long enough to resolve the internal spring-neap cycle. As a result, M_2 harmonic fits to the glider and mooring data (Section 3) are contaminated with S_2 variability. To acknowledge this, we refer to the estimated M_2 component of the co-located timeseries as D_2 following Alford et al. (2011). The comparative numerical model (Section 4.1) only includes the M_2 tidal constituent so we refer to model diagnostics as M_2.*'.

3) P4 L10. As you note the profile ends count as 1 observation. Only at the mid point are you doing better by a factor of 2. To clarify this point, the text has been changed to '*This yielded approximately 12 profiles (six independent samples near the surface and seabed; 12 independent samples at mid-depth) per semidiurnal tidal cycle.*'.

4) P4. Please explain up- and downsampling. Linear interpolation? Yes, linear interpolation is used for up- and downsampling. To specify this method, the text has been changed to '*linearly upsampled*' and '*linearly downsampled*'.

5) P7. Bottom friction plays an unclear role (for me at least) in the separation of barotropic and baroclinic. Friction applies to the total velocity and lowers the depth mean. Calculate rms difference for various depth mean flows. Yes, we agree that the frictional bottom boundary layer effects depth-mean velocity and so potentially causes a deviation from barotropic velocity. However, as the mooring did not have a near-bed downward-looking ADCP we cannot measure the near-bed velocity gradient. Data from the acoustic current meter (approximately 16 m above the bottom) do **not** show any substantial decrease in current velocity relative to the lowest bin of the ADCP (approximately 100 m above the bottom). We expect any error to be small compared to error from the linear interpolation and nearest neighbor extrapolation required to obtain full-depth velocity profiles. We state that '*barotropic velocity [is] assumed here to equal the depth-mean velocity*' to acknowledge this. We have also calculated the r.m.s. difference between the D_2 component of mooring depth-mean current velocity and the D_2 component of glider dive-average current (DAC) velocity. This is 1.2 cm s^{-1} and 0.8 cm s^{-1} in the along-slope and across-slope direction, respectively. These r.m.s. difference values have been included in Section 4.2, with maximum current velocity values for comparison.

6) Fig 3. Which mode has a phase shift near 550 m? Baroclinic modes and mode eigenspeeds are calculated from the observed buoyancy frequency profile and used to estimate the M_2 mode-1 horizontal wavelength over the WTR. This analysis shows that mode-1 horizontal velocity reverses at 505 m. A sentence has been added to the text, '*Mode-1 horizontal velocity, calculated from the observed buoyancy frequency profile, reverses at approximately 505 m, slightly above the pycnocline.*'.

7) Fig 4b should be solid lines according to caption- not interpolated. The phase profiles in Figure 4b have been changed to solid lines.

8) Fig 4c should have only a portion dashed- should be mostly solid. This confusion stems from the fact that solid/dashed line differentiation in the caption only applies to Figure 4d. To avoid this confusion, N^2 has been changed to a green line in Figure 4c.

9) Table 1. For angles you could use bearings. Done.

10) Section 4.1 has pretty good model-data comparison. Are you doing same or better than other models that you have referenced? Also on P17. All the studies of the FSC/WTR region that we reference used observational datasets [with the exception of Hall et al. (2011), which also has a numerical modelling component]. There have been other regional model studies, but these have tended to focus on mesoscale eddies (e.g., Oey, 1998) or the FBC and WTR overflows (e.g., Riemenschneider and Legg, 2007; Stashchuk et al., 2010). The internal tide studies by Gerkema (2002) and Hall et al. (2013) used simplified

2-D (x,z) numerical models and were both motivated by observations further northeast in the wider section of the FSC.

11) Fig 5a green flux vector is hard to see. The flux vector has been changed to a darker shade of green to distinguish it from the yellow contour shading beneath.

12) Fig 5. How about energy density from model compared to your observations? APE and HKE values for the observations and model are stated in Table 1 and compared in Section 4.1.

13) Fig 5. How was the magenta representative box decided? The dotted magenta box in Figure 5d encompasses all of the glider dives that were used to calculate the DAC tidal ellipse (deeper than 500 m). The figure caption has been changed to '*The magenta ellipse is calculated from DAC velocity and is representative of the area that contains all the dives deeper than 500 m (delineated by the dotted magenta line).*'.

14) P12 L25. Also gets you faster dives. This is typically true, but not always. It is possible to operate a Seaglider with a steep glide angle but low thrust. As Section 5 is on spatial sampling error, we feel that including a comment on temporal sampling may confuse the reader.

15) Fig 8. Use colour to highlight most relevant choice for these observations [in] Table 2 will be handy. An additional Monte Carlo case has been included (d/λ = 0.05) that is a close match to estimates for the WTR. This new case is used to estimate the glider sampling error for the observations, instead of interpolating between the d/λ = 0.03125 and d/λ = 0.0625. This new case is highlighted in red in Figure 8 and in bold in Table 2.

16) P18 L28. Explain the choice behind modal amplitude decay. The velocity amplitude decay rate, $u_n = u_1 e^{-0.5(n-1)}$, where n is mode number, results in an internal tide beam if velocity phase is equal for each baroclinic mode. The appendix text has been changed to '*Velocity amplitude decays with mode number, $u_n = u_1 e^{-0.5(n-1)}$, where u_1 is the mode-1 velocity amplitude. This decay rate results in a well-defined internal tide beam if velocity phase is approximately equal for each baroclinic mode. However, a different random set of baroclinic mode phases (ϕ_n) is used for each scenario simulated so internal tide beams are only apparent in a subset of scenarios. $u_1 = 0.28 \, m \, s^{-1}$ yields a mode-1 vertical isopycnal displacement amplitude of 50 m, but energy flux error and APE error are not sensitive to absolute amplitude.*'

Internal tide energy flux over a ridge measured by a co-located ocean glider and moored ADCP

Rob A. Hall[1], Barbara Berx[2], and Gillian M. Damerell[1]

[1]Centre for Ocean and Atmospheric Sciences, School of Environmental Sciences, University of East Anglia, Norwich Research Park, Norwich, NR4 7TJ, UK
[2]Marine Scotland Science, Marine Laboratory, 375 Victoria Road, Aberdeen, AB11 9DB, UK

Correspondence: Rob A. Hall (robert.hall@uea.ac.uk)

Abstract. Internal tide energy flux is an important diagnostic for the study of energy pathways in the ocean, from large-scale input by the surface tide, to small-scale dissipation by turbulent mixing. Accurate calculation of energy flux requires repeated full-depth measurements of both potential density (ρ) and horizontal current velocity ($\mathbf{u}$) over at least a tidal cycle and over several weeks to resolve the internal spring-neap cycle. Typically, these observations are made using full-depth oceanographic moorings that are vulnerable to being 'fished-out' by commercial trawlers when deployed on continental shelves and slopes. Here we test an alternative approach to minimise these risks, with $\mathbf{u}$ measured by a low-frequency ADCP moored near the seabed and ρ measured by an autonomous ocean glider holding station by the ADCP. The method is used to measure the ~~M_2~~ semidiurnal internal tide radiating from the Wyville Thompson Ridge in the North Atlantic. The observed energy flux (4.2 ± 0.2 kW m^{-1}) compares favourably with historic observations and a previous numerical model study.

Error in the energy flux calculation due to imperfect co-location of the glider and ADCP is estimated by sub-sampling potential density in an idealised internal tide field along pseudorandomly distributed glider paths. The error is considered acceptable ($<10\%$) if all the glider data is contained within a 'watch circle' with a diameter smaller than 1/8 the mode-1 horizontal wavelength of the internal tide. Energy flux is biased low because the glider samples density with a broad range of phase shifts, resulting in underestimation of vertical isopycnal displacement and available potential energy. The negative bias increases with increasing watch circle diameter. If watch circle diameter is larger than 1/8 the mode-1 horizontal wavelength, the negative bias is more than 3% and all ~~energy fluxes~~ realisations within the 95% confidence ~~limits~~ interval are underestimates. Over the Wyville Thompson Ridge, where the ~~M_2~~ semidiurnal mode-1 horizontal wavelength is ≈100 km and all the glider dives are within a 5 km diameter watch circle, the observed energy flux is estimated to have a negative bias of only ~~0.5~~0.4% and an error ~~less than 4~~of less than 3% at the ~~99~~95% confidence limit. With typical glider performance, we expect energy flux error due to imperfect co-location to be $<10\%$ in most mid-latitude shelf slope regions.

1 Introduction

Internal tides are a ubiquitous hydrodynamic feature over continental shelves and slopes as they are commonly generated at the shelf break by across-slope tidal flows (Baines, 1982; Pingree et al., 1986; Sharples et al., 2007). However, direct measurement of internal tides can be a challenge in these regions due to intense commercial fishing activity leading to an increased risk of oceanographic mooring loss (Sharples et al., 2013). Calculation of internal tide energy flux, a key diagnostic for the understanding of baroclinic energy pathways, requires repeated full-depth measurements of both potential density (ρ) and horizontal current velocity ($\mathbf{u}$) over at least a tidal cycle (Nash et al., 2005). If an objective is to resolve the internal spring-neap cycle or observe the effect of seasonal changes in stratification on the internal tide field, repeated full-depth measurements over several weeks or months are required. Typically, these measurements are made using a full-depth oceanographic mooring incorporating an acoustic Doppler current profiler (ADCP) and a string of conductivity-temperature loggers (e.g., Hopkins et al., 2014), or a profiling mooring with a CTD and acoustic current meter (e.g., Zhao et al., 2012). On continental shelves and slopes, these full-depth moorings are vulnerable to being 'fished-out' by demersal and pelagic trawling activity.

Hall et al. (2017b) describe a novel alternative approach to minimise these risks, with $\mathbf{u}$ measured by a low-frequency ADCP moored near the seabed and ρ measured by an autonomous ocean glider holding station by the ADCP as a 'virtual mooring'. Commercial fishing activity on continental shelves and their adjacent slopes is often intense because these regions are highly biologically productive. However, steps can be taken to reduce the risk of ADCP loss, including deploying deeper than 600 m, keeping mooring lines short, or using trawl-resistant frames. Being relatively small, gliders are unlikely to be fished-out, and the risk can be further reduced by real-time evasive action in response to vessel proximity guided by the maritime Automatic Identification System (AIS). However, this alternate approach was not comprehensively tested by Hall et al. (2017b) because of glider navigation and telemetry problems. In this study we test the method using a co-located glider and ADCP dataset from the Wyville Thompson Ridge in the North Atlantic, a topographic feature that previous observations and numerical model studies suggest is an energetic internal tide generator (Sherwin, 1991; Hall et al., 2011). We also estimate the error in the energy flux calculation due to imperfect co-location of the glider and ADCP and find that, with typical glider performance, it is acceptable in most mid-latitude shelf slope regions~~with typical glider performance~~.

Ocean gliders have previously been used to observe internal waves and internal tides (Rudnick et al., 2013; Rainville et al., 2013; Johnston and Rudnick, 2015; Boettger et al., 2015; Hall et al., 2017a), including the calculation of energy fluxes using current velocity measurements from gliders equipped with ADCPs (Johnston et al., 2013, 2015). However, ADCPs are not routinely integrated with commercially available glider platforms (Seaglider, Slocum, and SeaExplorer), in part due to their higher power requirement. Synergy with moored ADCP data allows accurate calculation of internal tide energetics without the endurance limitations and data analysis complexities of an ADCP-equipped glider (e.g., Todd et al., 2017).

In Section 2 the temporal resolution constraints of glider ~~measurments~~ measurements are explained and the observations used in this study described. The calculation of internal tide energy flux from co-located glider and moored ADCP data is fully described in Section 3. Observations of the internal tide radiating from the Wyville Thompson Ridge are presented in
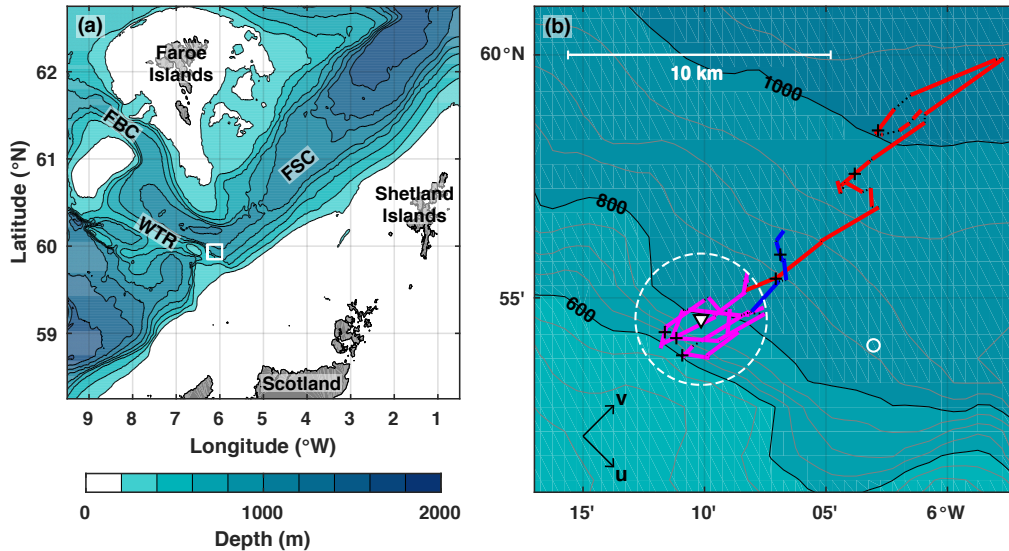
Figure 1. (a) Location of the experiment site (white square) and regional bathymetry, including the Faroe Bank Channel (FBC), Faroe-Shetland Channel (FSC), and Wyville Thompson Ridge (WTR). (b) Path of the glider over the WTR with local bathymetry (Δ50-m isobaths in grey). Dives are separated into deployment (red), on-station (magenta), and recovery (blue) sections with a black cross every 12 hours (00:00 and 12:00 UTC). The dotted black lines are surface drift. The white triangle is the location of the ADCP mooring and the dashed white line delineates a 5-km diameter 'watch circle' around it. The ~~green~~ white circle is the location of the CTD repeat station where Sherwin (1991) observed a semidiurnal internal tide. The bathymetric dataset is the GEBCO 2014 30 arc-second grid (http://www.gebco.net).

Section 4 and compared with historic observations and a previous numerical model study. In Section 5 the error in the energy flux calculation due to imperfect co-location is estimated. Key results are summarised and discussed in Section 6.

2 Observations

High temporal resolution is crucial for internal tide observations; Nash et al. (2005) suggest a minimum of four evenly-
5   distributed independent profiles of **u** and ρ are required per tidal cycle for an unbiased calculation of energy flux. Over conti-
nental shelves and upper shelf slopes, this temporal resolution is achievable using gliders. Typical glider vertical velocities are
15-20 cm s^{-1}, so a complete dive cycle to 1000 m can take as little as three hours. This yields eight profiles (four dives) per
semidiurnal ($\approx$12-hour) tidal cycle, but near the surface and seabed the descending and ascending profiles converge in time so
the number of independent samples is halved to four. For diurnal ($\approx$24-hour) internal tides, 16 profiles per cycle are possible.
10   In shallower water the temporal resolution of glider measurements increases further; 40-minute full-depth dives are achievable
over a 200-m deep shelf break, yielding 36 profiles per semidiurnal tidal cycle. The depth-limiting factor of the methodology is
the range of the ADCP. In narrowband mode, 75 kHz ADCPs have a maximum range of around 600 m (dependent on environ-

mental conditions) so multiple ADCPs or additional current meters on the mooring line are required for sites between 600 m and 1000 m deep.

The observations used to test the method were collected from the northern flank of the Wyville Thompson Ridge (WTR) in the North Atlantic (Fig. 1a). A Kongsberg Seaglider (SG613; Eriksen et al., 2001) was deployed from NRV *Alliance* between 2nd and 5th June 2017 during the fourth Marine Autonomous Systems in Support of Marine Observations mission (MASSMO4). The glider was navigated from the deeper waters of the Faroe-Shetland Channel (FSC) to the WTR and held

5   station for 40 hours ~~over~~ by a short oceanographic mooring, deployed five days previously from MRV *Scotia* (Fig. 1b). The mooring was sited close to the 800 m isobath and instrumented with an upwards-looking 75 kHz RDI Long Ranger ADCP at approximately 722 m and an Aanderaa Seaguard acoustic current meter at 784 m, yielding observations of horizontal current velocity over 78% of the water column. When on-station by the ADCP mooring, the glider made repeated 2-hour dives to 700 m or the seabed, whichever was shallower. This yielded approximately 12 profiles (six independent samples near the

10   surface and seabed; 12 independent samples at mid-depth) per semidiurnal tidal cycle.

Glider location at the surface, before and after each dive, was given by GPS position. Subsurface sample locations were approximated by linearly interpolating surface latitude and longitude onto sample time. When on-station, the glider stayed within 2.5 km of the mooring and the mean horizontal distance between temporally coincident glider and ADCP measurements was 1.3 km. This spatial scattering of the glider data is small compared to the semidiurnal mode-1 horizontal wavelength over

15   the WTR ($\approx$100 km, calculated from the observed buoyancy frequency profile) and so the glider data are initially considered a fixed-point timeseries with no spatial-temporal aliasing.

As the glider was on-station for only 40 hours, the co-located timeseries is not long enough to resolve the internal spring-neap cycle. As a result, M_2 harmonic fits to the glider and mooring data (Section 3) are contaminated with S_2 variability. To acknowledge this, we refer to the estimated M_2 component of the co-located timeseries as D_2 following Alford et al. (2011).

20   The comparative numerical model (Section 4.1) only includes the M_2 tidal constituent so we refer to model diagnostics as M_2.

2.1   Data processing

The glider was equipped with a standard Sea-Bird Electronics conductivity-temperature (CT) sail sampling at 0.2 Hz and the data processed using the UEA Seaglider Toolbox (https://bitbucket.org/bastienqueste/uea-seaglider-toolbox) following Queste

25   (2014). Conductivity data were corrected for thermal hysteresis following Garau et al. (2011) and the Seaglider flight model regressed using a method adapted from Frajka-Williams et al. (2011). As the CT sail was unpumped, salinity samples were flagged when the glider's speed was less than 10 cm s^{-1} or it was within 8 m of apogee[1]. Temperature-salinity profiles from descents and ascents were independently averaged (median value) in 5-m depth bins, typically with 4-5 samples per bin. Sample time was averaged into the same bins to allow accurate temporal analysis at all depths. Absolute salinity (S_A), conservative

30   temperature (Θ), and potential density (ρ) in each bin were calculated using the TEOS-10 equation of state (IOC et al., 2010).

---

[1]Apogee is the phase of the dive between descent and ascent, when the glider pitches upwards ~~and~~ increases ~~it~~ its buoyancy. Flow through the conductivity cell is unpredictable during this phase and so salinity spikes are common.
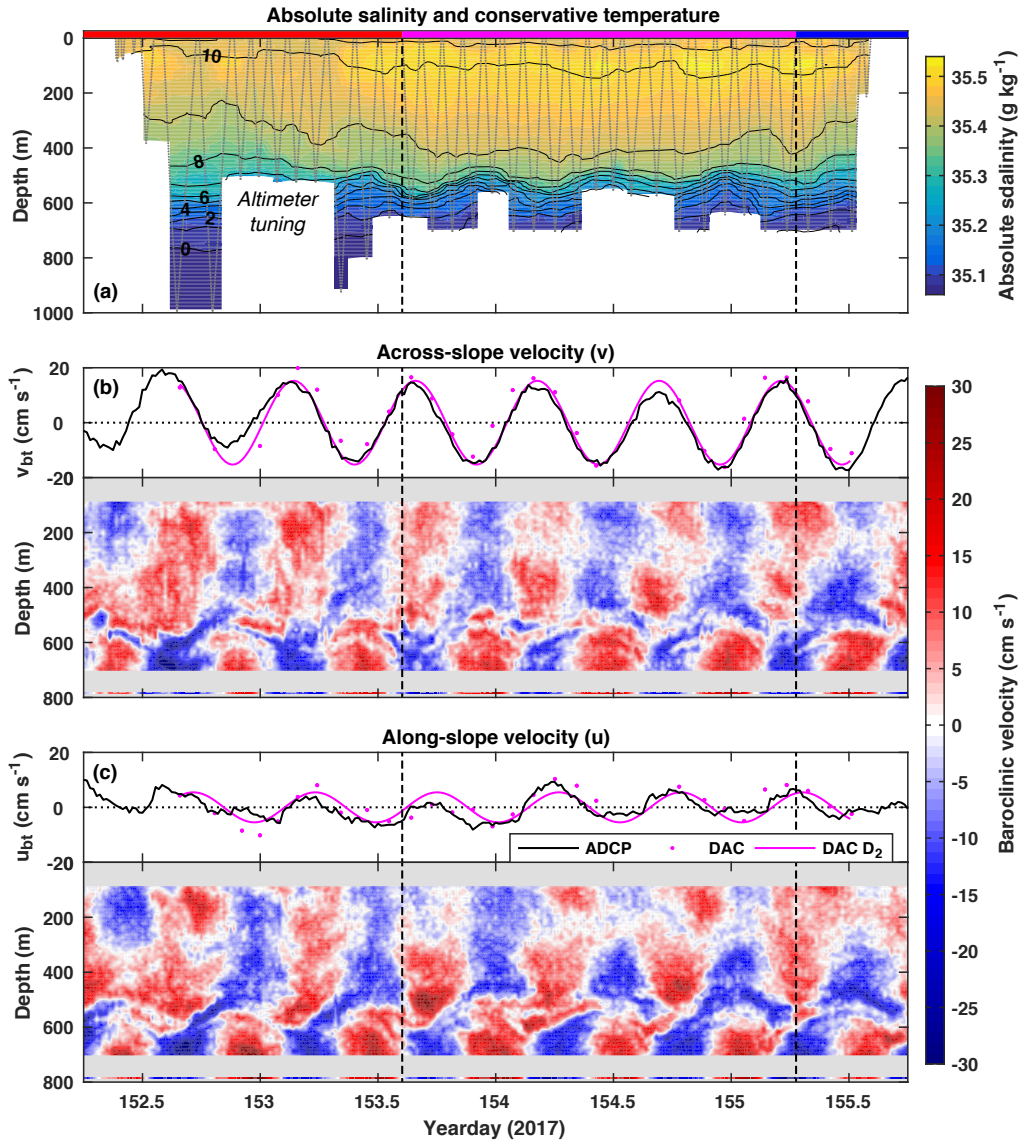
Figure 2. (a) Absolute salinity (colour) and conservative temperature (black contours, interval: 1 °C) measured by the glider. The dotted grey line is the glider's path and shows the temporal sampling resolution. The magenta section is when the glider was ~~on station~~ on-station by the ADCP mooring. (b) Across-slope barotropic (black line) and baroclinic (colour) velocity measured by the ADCP/current meter and dive-average current (DAC) velocity inferred from the glider (magenta dots). The magenta line is ~~an M_2~~ a D_2 harmonic fit to DAC velocity. Positive velocities are northeast (down-slope). (c) is as (b) but for along-slope velocities. Positive velocities are southeast.

The 75 kHz ADCP was configured in narrowband mode with 10-m bins and 24 pings per 20-minute ensemble. The ADCP data were processed using Marine Scotland Science's standard protocols, including correction for magnetic declination and quality assurance based on error velocity, vertical velocity, and percentage good ping thresholds. The ADCP data were then linearly upsampled onto the same Δ5-m depth levels as the glider data. The acoustic current meter was configured with a 10-minute sampling interval and linearly downsampled onto the same 20-minute sampling interval as the ADCP. Good velocity data were recovered for all depths levels between 85 m and 705 m, as well as 780-785 m. In addition to the ADCP/current meter measurements, horizontal velocity was inferred from GPS position and the Seaglider flight model using a dive-average current method (DAC; Eriksen et al., 2001; Frajka-Williams et al., 2011). DAC was only calculated for dives deeper than 500 m so that values were representative of the majority of the water column. All velocities were transformed into along-slope and across-slope components. We take the ~~of the~~ northern flank of the WTR to be orientated exactly northwest-southeast so along-slope (u) is positive southeast and across-slope (v) is positive northeast (down-slope).

The full 3-day glider timeseries of conservative temperature and absolute salinity is shown in Figure 2a. A semidiurnal internal tide is evident as a vertical oscillation of the main pycnocline (centred around 550 m) with an amplitude up to 50 m and a period of $\approx$12 hours. Temporally coincident ADCP/current meter ~~measurments~~ measurements (Fig. 2b,c) show dominant semidiurnal periodicity and a reversal of baroclinic current velocity across the main pycnocline, characteristic of a low-mode internal tide. Mode-1 horizontal velocity, calculated from the observed buoyancy frequency profile, reverses at approximately 505 m, slightly above the pycnocline.

3 Internal tide energy flux

Following Kunze et al. (2002) and Nash et al. (2005), internal tide energy flux is calculated $\mathbf{F} = \langle \mathbf{u}'_{bc} p' \rangle$. The method requires repeated full-depth measurements of ρ and $\mathbf{u}$ over at least a tidal cycle in order to determine pressure perturbation (p') and baroclinic velocity ($\mathbf{u}'_{bc}$), respectively.

3.1 Pressure perturbation

For the 40-hour window when the glider was on-station by the ADCP mooring, potential density anomaly is calculated by subtracting the window-mean density profile from measured potential density,

$$\rho'(z,t) = \rho(z,t) - \overline{\rho}(z). \tag{1}$$

Before subtraction, $\overline{\rho}(z)$ is smoothed with a 50-m gaussian tapered running mean ($\sigma = 10$ m) to yield a suitable background density profile. Vertical isopycnal displacement is then calculated

$$\xi(z,t) = -\rho'(z,t) \left(\frac{\partial \overline{\rho}}{\partial z} \right)^{-1}. \tag{2}$$

To separate ~~semidiurnal~~ D_2 internal tide variability from other physical processes, M_2 tidal period (T = 12.42 hours) harmonics are fit to ξ on each Δ5-m depth level following Emery and Thomson (2001). This analysis is only applied to depth levels
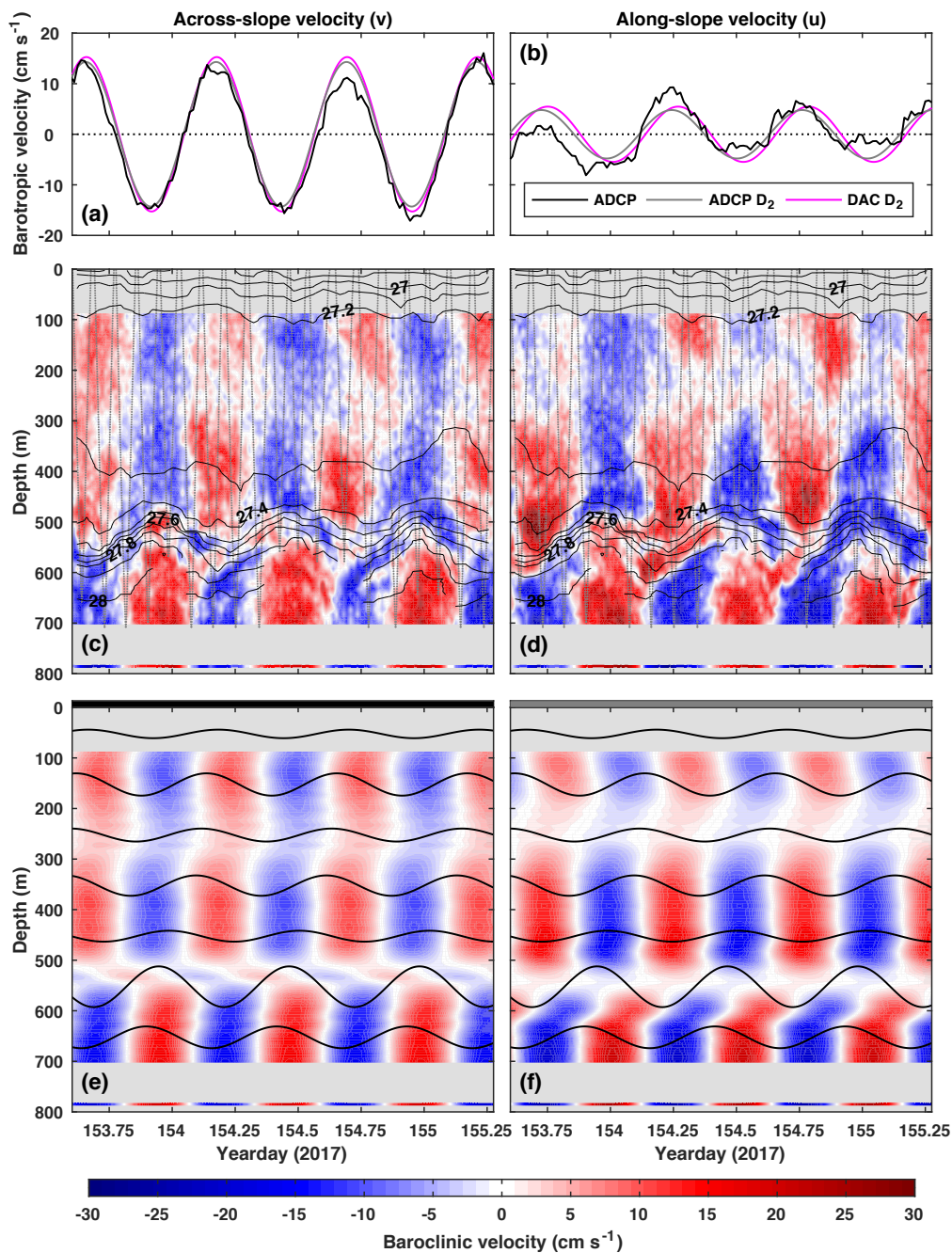
Figure 3. (a) Across-slope barotropic velocity (black), the D_2 component (grey), and a D_2 harmonic fit to DAC velocity (magenta). (c) Across-slope baroclinic velocity (colour) overlaid with potential density (black contours, interval: 0.1 kg m^{-3}). (e) The D_2 component of across-slope baroclinic velocity (colour) overlaid with the D_2 component of vertical isopycnal displacement every 100 m (black lines). (b), (d) and (f) are as (a), (c) and (e) but for along-slope velocities.
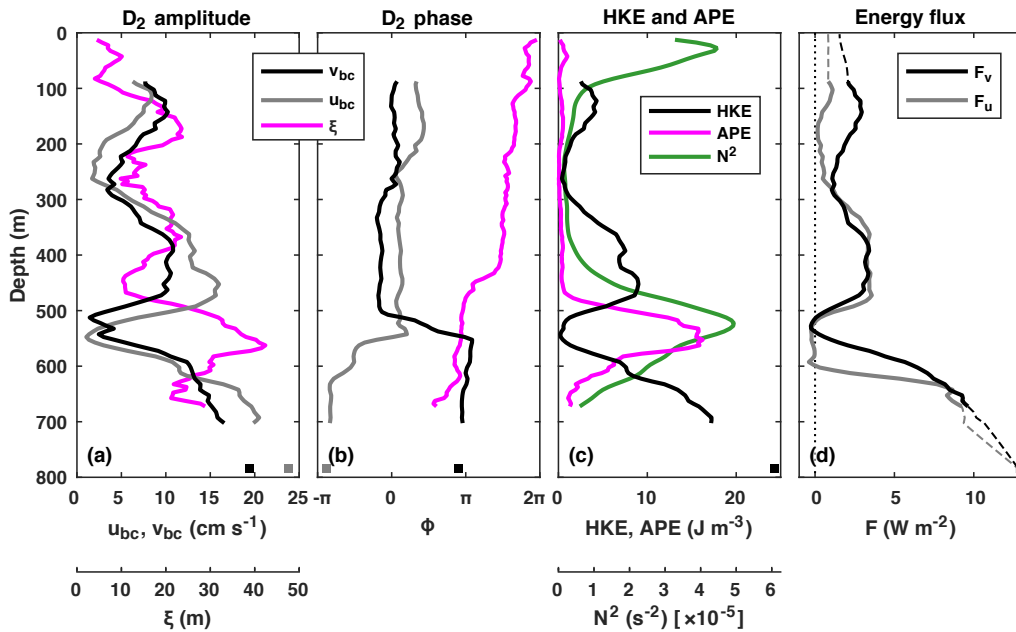
7

Figure 4. (a) Amplitude and (b) phase of the D_2 components of across-slope baroclinic velocity (black), along-slope baroclinic velocity (grey), and vertical isopycnal displacement (magenta). (c) Horizontal kinetic energy (black), available potential energy (magenta), and buoyancy frequency squared (green). (d) Across-slope (black) and along-slope (grey) D_2 internal tide energy flux. Solid lines indicate both glider and ADCP data coverage; dashed lines indicate that one or both of the datasets required extrapolation. Positive fluxes are down-slope and along-slope to the southeast.

between 10 m and 675 m; near-surface and near-bottom bins are excluded because of high numbers of flagged samples and reduced temporal resolution due to the glider going into apogee above 700 m. To obtain a full-depth timeseries, the $\cancel{M_2}$ D_2 component of ξ is linearly extrapolated assuming $\xi = 0$ at the surface ($z = 0$) and bottom ($z = -H$, where H is water depth). Buoyancy frequency squared, $N^2 = -g/\rho_0(\partial\overline{\rho}/\partial z)$ is also linearly extrapolated, assuming $N^2 = 10^{-6}$ s^{-2} at the surface and

5 bottom. Pressure perturbation is then calculated by integrating the hydrostatic equation from the surface,

$$p'(z,t) = p'_{\text{surf}}(t) + \rho_0 \int_z^0 N^2(z)\xi(z,t)\,dz, \tag{3}$$

where p'_{surf} is pressure perturbation at the surface due to the internal tide, determined by applying the baroclinicity condition for pressure,

$$p'_{\text{surf}}(t) = -\frac{1}{H} \int_{-H}^0 p'(z,t)\,dz. \tag{4}$$

Figure 3 shows potential density (panels c and d) and the ~~M_2~~ D_2 component of vertical isopycnal displacement (panels e and f) for the 40-hour analysis window. The amplitudes and phases of the ~~M_2~~ D_2 component of ξ are shown in Figure 4a,b.

~~(a) Across-slope barotropic velocity (black), the M_2 component (grey), and an M_2 harmonic fit to DAC velocity (magenta). (c) Across-slope baroclinic velocity (colour) overlaid with potential density (black contours, interval: 0.1 kg m^{-3}). (e) The M_2 component of across-slope baroclinic velocity (colour) overlaid with the M_2 component of vertical isopycnal displacement every 100 m (black lines). (b), (d) and (f) are as (a), (c) and (e) but for along-slope velocities.~~

3.2 Baroclinic velocity

For the same 40-hour window, horizontal velocity perturbation is calculated

$$\mathbf{u}'(z,t) = \mathbf{u}(z,t) - \overline{\mathbf{u}}(z), \tag{5}$$

where $\overline{\mathbf{u}}(z)$ is the window-mean horizontal velocity profile. There are three spatial gaps in the timeseries: above 85 m, between the ADCP and current meter (705-780 m including blanking distance), and from the current meter to the seabed (785-800 m). To obtain a full-depth timeseries, $\mathbf{u}'$ is linearly interpolated between the ADCP and current meter, and extrapolated to the surface and the bottom using a nearest neighbour method. Baroclinic velocity is then calculated

$$\mathbf{u}'_{\mathrm{bc}}(z,t) = \mathbf{u}'(z,t) - \mathbf{u}'_{\mathrm{bt}}(t), \tag{6}$$

where $\mathbf{u}'_{\mathrm{bt}}$ is barotropic velocity, assumed here to equal the ~~depth-average~~ depth-mean velocity, calculated

$$\mathbf{u}'_{\mathrm{bt}}(t) = \frac{1}{H} \int_{-H}^{0} \mathbf{u}'(z,t)\,dz. \tag{7}$$

The ~~M_2~~ D_2 components of $\mathbf{u}'_{\mathrm{bc}}$ and $\mathbf{u}'_{\mathrm{bt}}$ are extracted using the same harmonic analysis method applied to ξ. Figure 3 shows barotropic (a and b) and baroclinic (c and d) velocity and the ~~M_2~~ D_2 components of barotropic (a and b) and baroclinic (e and f) velocity for the 40-hour analysis window. The amplitudes and phases of the ~~M_2~~ D_2 component of $\mathbf{u}'_{\mathrm{bc}}$ are shown in Figure 4a,b.

3.3 Internal tide energetics

Profiles of internal tide energy flux, available potential energy (APE), and horizontal kinetic energy (HKE) are calculated

$$\mathbf{F}(z) = \langle \mathbf{u}'_{\mathrm{bc}}(z,t)p'(z,t)\rangle, \tag{8}$$

$$\mathrm{APE}(z) = \frac{1}{2}\rho_0 N^2(z)\langle \xi^2(z,t)\rangle, \text{ and} \tag{9}$$

$$\mathrm{HKE}(z) = \frac{1}{2}\rho_0 \langle \mathbf{u}'^2_{\mathrm{bc}}(z,t)\rangle, \tag{10}$$

where $\langle \cdot \rangle$ denotes an average (mean) over an integer number of M_2 ~~tidal~~ cycles and $\rho_0 = 1028$ kg m^{-3} is a reference density.

5 4   Results

~~(a) Amplitude and (b) phase of the M_2 components of across-slope baroclinic velocity (black), along-slope baroclinic velocity~~
~~(grey), and vertical isopycnal displacement (magenta). (c) Horizontal kinetic energy (black), available potential energy (magenta),~~
~~and buoyancy frequency squared (grey dashed). (d) Across-slope (black) and along-slope (grey) M_2 internal tide energy flux.~~
~~Solid lines indicate both glider and ADCP data coverage; dashed lines indicate that one or both of the datasets required~~
10 ~~extrapolation. Positive fluxes are down-slope and along-slope to the southeast.~~

~~Variable Units Glider ADCP Model F_u kW m^{-1} 3.35 F_v kW m^{-1} 3.00 F_{mag} kW m^{-1} 4.50 F_{dir} ° −3.2 HKE kJ m^{-2} -~~
~~5.50 4.99 APE kJ m^{-2} 1.73 - 2.24 ξ_{max} m 42.4 - 41.1 N^2_{max} s^{-2} ×10^{-5} 4.9 - 5.8 Semi-major axis cm s^{-1} 15.5 14.7 21.1~~
~~(2.2) Semi-minor axis cm s^{-1} 4.8 3.5 2.5 (0.7) Inclination ° 35.0 31.7 30.6 (1.8) Phase ° 331.4 329.6 - Comparison between~~
~~observed (glider and ADCP) and modelled internal tide and surface tidal ellipse diagnostics. All values are for the M_2 tide.~~
15 ~~Modelled ellipse values are averaged (mean) over 48 grid-points representative of the area travelled by the glider. The values~~
~~in brackets are standard deviations. All angles are counter-clockwise from east.~~

~~Maximum M_2~~ Maximum D_2 vertical isopycnal displacement is 42 m and occurs at 565 m (Fig. 4a), within the main pycnocline. This is comparable with historic observations of a semidiurnal internal tide over the northern flank of the WTR. Sherwin (1991) analysed CTD data from a 17-hour repeat station (30 minutes between casts) that was 6.7 km east of the
20 mooring (Fig. 1b) and determined maximum ~~M_2~~ D_2 vertical isopycnal displacement to be 37 m at 580 m, again within the pycnocline. Here, almost all APE is contained within the pycnocline (Fig. 4c), because maximum ξ occurs at a similar depth to maximum N^2 (4.9×10^{-5} s^{-2} at 525 m). ~~M_2~~ D_2 baroclinic velocity is maximum ($\approx$20 cm s^{-1}) near-bottom (Fig. 4a), as is HKE (Fig. 4c). Depth-integrated HKE and APE are 5.5 kJ m^{-2} and 1.7 kJ m^{-2}, respectively.

Both the across- and along-slope components of ~~M_2~~ D_2 internal tide energy flux are maximum ($\approx$12.7 kW m^{-2}) near-
25 bottom and go to zero at the depth of maximum N^2 (Fig. 4d), characteristic of a low-mode internal tide with a pycnocline in the lower half of the water column. Depth-integrated energy flux magnitude is 4.2 kW m^{-1}, directed almost due east (7° counter-clockwise from east). In comparison, Sherwin (1991) estimated the ~~M_2~~ D_2 mode-1 internal tide energy flux at the nearby CTD repeat station to be 4.7 kW m^{-1}, but was unable to diagnose the direction.

4.1   Model comparison

30 In Figure 5 the observations are compared with the regional tide model described by Hall et al. (2011). The model is a configuration of the Princeton Ocean Model (POM; Blumberg and Mellor, 1987) for the FSC and WTR region, initiated with typical late-summer stratification, and forced at the boundaries with M_2 barotropic velocities (see Hall et al., 2011, for full details). Maximum N^2 in the model is slightly higher than observed (Table 1), but the vertical distribution of stratification is similar with the main pycnocline between 500 m and 600 m. M_2 internal tide generation occurs within the model domain, driven by barotropic tidal currents across isobaths, and is diagnosed as positive barotropic-to-baroclinic energy conversion (Fig. 5b). The northern flank of the WTR is an area of energetic internal tide generation, up to 4 W m^{-2}, and radiates an
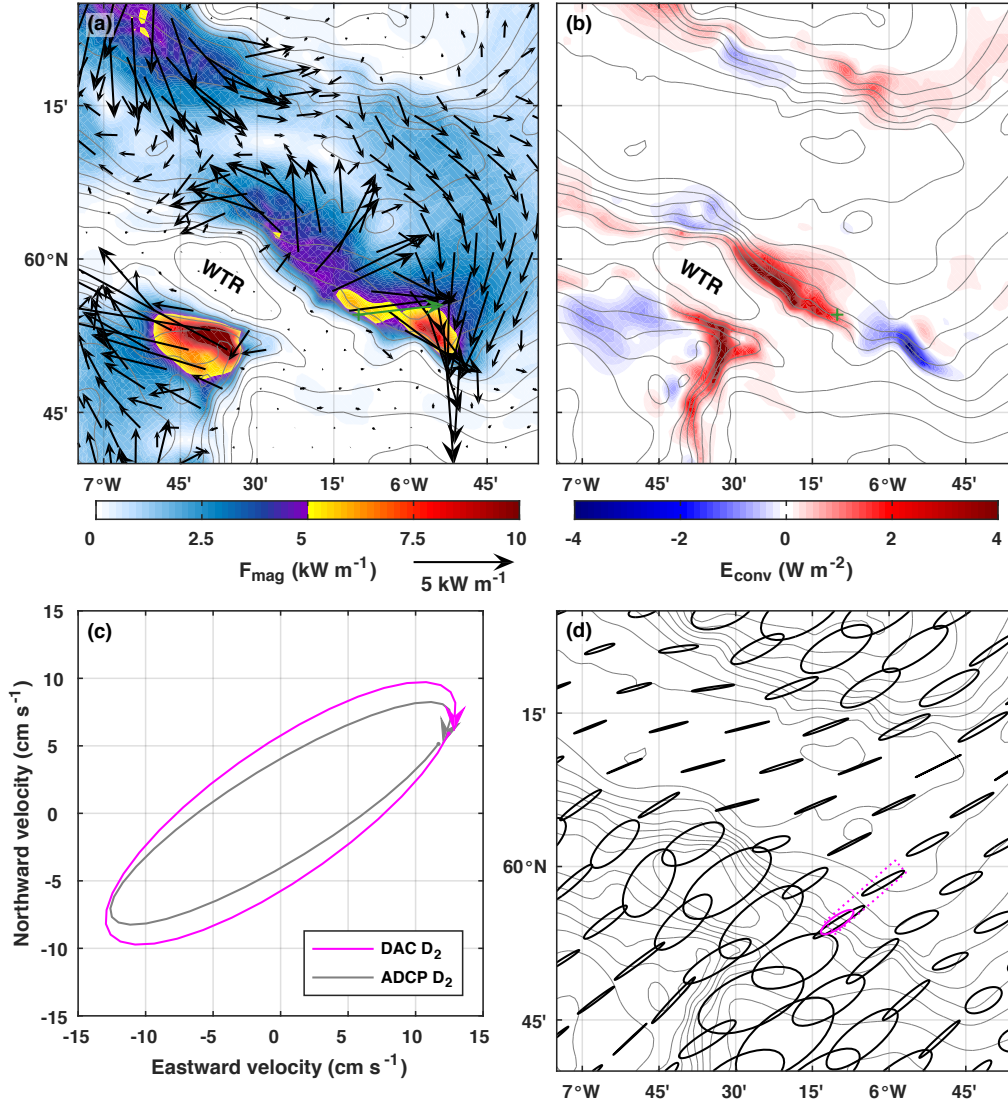
Figure 5. (a) Depth-integrated M_2 internal tide energy flux from the regional tide model described by Hall et al. (2011). Vectors are plotted every five grid points (5 km) in each direction. The underlying colour is the energy flux magnitude. The green vector is the depth-integrated ~~M_2~~ D_2 internal tide energy flux observed at the green cross. (b) Barotropic-to-baroclinic M_2 energy conversion from the model. (c) ~~M_2~~ D_2 surface ellipses calculated from glider-inferred DAC velocity (magenta) and ADCP-measured barotropic velocity (grey). (d) M_2 surface ellipses, every ten grid points (10 km) in each direction, from the model. The magenta ellipse is calculated from DAC velocity and is representative of the area that contains all the dives deeper than 500 m (delineated by the ~~magenta~~ dotted magenta line). The bathymetry contour interval is 100 m.

Variable	Units	Glider	ADCP	Model
F_u	kW m^{-1}	2.62		3.35
F_v	kW m^{-1}	3.31		3.00
F_{mag}	kW m^{-1}	4.23		4.50
F_{dir}	°	6.7		-3.2
HKE	kJ m^{-2}	-	5.50	4.99
APE	kJ m^{-2}	1.73	-	2.24
ξ_{max}	m	42.4	-	41.1
N^2_{max}	s^{-2} [$\times 10^{-5}$]	4.9	-	5.8
Semi-major axis	cm s^{-1}	15.5	14.7	21.1 (2.2)
Semi-minor axis	cm s^{-1}	4.8	3.5	2.5 (0.7)
Inclination	°	35.0	31.7	30.6 (1.8)
Phase	°	331.4	329.6	-

Table 1. Comparison between observed (glider and ADCP) D_2 and modelled M_2 internal tide and surface tidal ellipse diagnostics. Modelled ellipse values are averaged (mean) over the 48 grid-points in the area that contains all the glider dives deeper than 500 m (see Fig. 5d). The values in brackets are standard deviations. All bearings are counter-clockwise from east.

internal tide into the southern FSC. Modelled internal tide energy fluxes are spatially variable, but >5 kW m^{-1} at some locations (Fig. 5a). The mooring was located east of the most energetic generation and up-slope of the largest energy fluxes.

For direct comparison, the model output is interpolated onto the exact location of the mooring (Table 1). The modelled M_2 internal tide energy flux is 6-7% larger than the observed D_2 energy flux, but within 10° of its direction. Maximum modelled vertical isopycnal displacement is 41 m (slightly smaller than observed), but is compensated by the higher maximum N^2 and results in modelled APE being 30% larger than observed; modelled HKE is 10% smaller than observed.

4.2 Surface tidal ellipses

As well as measuring potential density by the ADCP mooring, the glider is used to infer a second estimate of barotropic velocity. Harmonic analysis is used to extract the ~~M_2~~ D_2 component of DAC velocity (all dives deeper than 500 m) and compared to the ~~M_2~~ D_2 component of $\mathbf{u}'_{\mathrm{bt}}$ from the ADCP/current meter. Barotropic velocity is highest in the across-slope direction (maximum 15 cm s^{-1}, Fig. 3a) and there is a very close match between the DAC and ADCP estimates ~~.~~ (r.m.s. difference is 0.8 cm s^{-1}). In the along-slope direction, where barotropic velocity is lower ~~,~~ (maximum 0.5 cm s^{-1}, Fig. 3b), the DAC estimate lags the ADCP estimate by 35 minutes, but their amplitudes closely match (~~Fig. 3b~~r.m.s. difference is 1.2 cm s^{-1}). The resulting surface tidal ellipses have similar semi-major axis lengths and phases (Table 1), but the DAC estimate is less eccentric (more circular) and rotated ~~a further~~ 3° counter-clockwise (Fig. 5c). Compared with M_2 surface ellipses from the regional tide model described by Hall et al. (2011), both observational estimates are less eccentric and have shorter semi-major axes (Table 1;
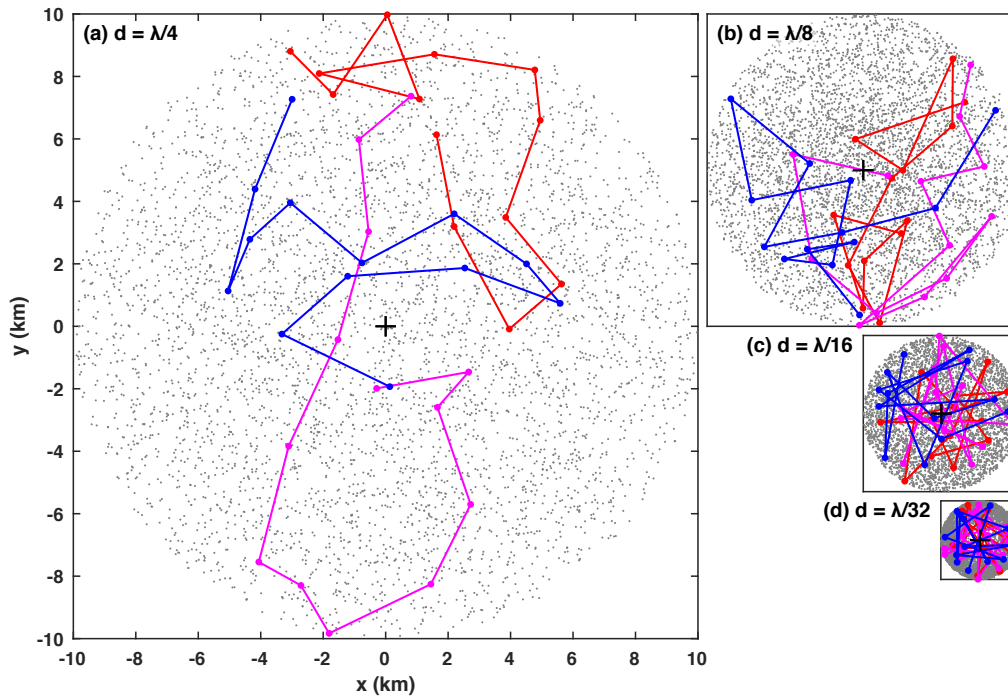
Figure 6. Pseudorandomly distributed glider paths within watch circles of diameter (a) 1/4λ, (b) 1/8λ, (c) 1/16λ, and (d) 1/32λ. The first 5000 surface locations are shown with a grey dot and the first three twelve-dive scenarios are shown in colour. The black cross is the location of the ADCP at the centre of the watch circle. All four panels are the same scale.

5   Fig. 5c). However, the inclination of observed and modelled ellipses are comparable, with their semi-major axes orientated across-slope. This is the orientation required to generate an energetic internal tide at the WTR.

5   Glider sampling error

The separation of spatial and temporal variability is a common problem when interpreting glider data due to their slow speed (Rudnick and Cole, 2011) and imperfect positioning. In this context, the inability of the glider to perfectly hold station by the

10   ADCP mooring leads to error in the calculation of internal tide energy flux (Section 3) due to mis-sampling of the spatially and temporally varying density field. An understanding of this error is important for both mission planning and interpretation of results. Other missions along the European continental slope (e.g., Hall et al., 2017a) have shown that a glider operating as a virtual mooring by repeatedly diving to 1000 m around a fixed station can maintain a 'watch circle' with a diameter of approximately 5 km, i.e., all dives start and end within 2.5 km of the target location. The ability to do this is dependent on environmental conditions, particularly tidal and slope currents, but the lower limit is effectively set by the glide angle; a steep, 45° glide angle will result in around 2 km horizontal travel over a complete dive cycle to 1000 m.

5   The size of the energy flux error is related to the length-scale of the sampling cloud (d, the diameter of the watch circle) and the horizontal wavelength of internal tide being measured (λ). If $d \ll \lambda$ we can consider the glider data a fixed-point timeseries with no spatial-temporal aliasing, and so the error will be small. As d increases the glider will increasingly sample density at the wrong phase of the internal tide and so the error will increase because the measured pressure perturbation (p'_{Glider}) will deviate from the pressure perturbation at the ADCP (p'_{ADCP}), located at the centre of the watch circle. If $d \simeq \lambda$ the glider will
10   sample density at random phases of the internal tide and so p'_{Glider} and p'_{ADCP} will be uncorrelated.

Here we use a Monte Carlo approach to estimate the energy flux error. Potential density in an idealised internal tide field is sub-sampled along pseudorandomly distributed glider paths contained within watch circles of varying diameters. The 'true' depth-integrated energy flux at the ADCP, $\mathbf{F}_{\text{true}} = \int_{-H}^{0} \langle \mathbf{u}'_{\text{bc}} p'_{\text{ADCP}} \rangle \, dz$, is then compared with the 'observed' depth-integrated energy flux, $\mathbf{F}_{\text{obs}} = \int_{-H}^{0} \langle \mathbf{u}'_{\text{bc}} p'_{\text{Glider}} \rangle \, dz$. In both equations $\mathbf{u}'_{\text{bc}}$ is baroclinic velocity at the ADCP. An idealised M_2 multi-
15   mode internal tide field is created for a 1000-m deep water column with uniform stratification (Appendix A). The mode-1 horizontal wavelength (λ) is 80 km and mode-1 vertical isopycnal displacement is 50 m, typical of mid-latitude shelf slope regions. Glider sampling is modelled as a group of twelve 1000-m dives, over 37 hours ($\approx$3 M_2 cycles), within a watch circle of diameter d. Each dive is 2 hours 50 minutes long, with 15 minutes at the surface between dives. Horizontal distance travelled during each dive cycle is between 1.5 km and 4 km (typical of real glider missions), but there is no surface drift. The glider's
20   path during each dive is determined by randomly selecting a start position within the watch circle then randomly selecting an end position 1.5-4 km away, but still within the watch circle. The start position of the following dive is the same as the end position. Potential density is linearly interpolated onto this pseudorandom glider path and the resulting density 'observations' analysed using the method described in Section 3.1 to yield p'_{Glider}.

~~Eight~~ Nine cases are investigated, with d ranging from $\lambda/32$ (2.5 km) to $\lambda/4$ (20 km), and for each case 5000 differ-
25   ent twelve-dive scenarios are simulated. A different random set of baroclinic mode phases is used for each scenario. Example pseudorandomly distributed glider paths for four cases are shown in Figure 6. Energy flux relative error is defined $\mathbf{F}_{\text{err}} = (\mathbf{F}_{\text{obs}} - \mathbf{F}_{\text{true}})/\mathbf{F}_{\text{true}}$, so positive error indicates an overestimation and negative error indicates an underestimation. Similarly, APE relative error is defined $\text{APE}_{\text{err}} = (\text{APE}_{\text{obs}} - \text{APE}_{\text{true}})/\text{APE}_{\text{true}}$, where APE_{true} is 'true' depth-integrated APE (calculated from ξ_{ADCP}) and APE_{obs} is 'observed' depth-integrated APE (calculated from ξ_{Glider}).

30   ## 5.1   Single-scenario example

A single-scenario for the $d = \lambda/4$ case is shown in Figure 7 to highlight the impact of mis-sampling density on observed energy flux and APE. This is an extreme example, with all the glider dives 6-10 km from the ADCP (~~Figure~~Fig. 7d), and features near-bottom internal tide intensification similar to observed on the northern flank of the WTR. In this example, the error in measured density is maximum in the lower half of the water column (where ξ_{ADCP} is up to 80 m; Fig. 7a,b); the resulting ξ_{Glider} underestimates ξ_{ADCP} by up to 20 m and leads by up to 40 minutes. Observed energy flux and APE underestimate true energy flux and APE over the majority of the water column (Fig. 7c) and, depth-integrated, underestimate by 772 W m^{-1} ($\mathbf{F}_{\text{err}} = -0.09$) and 615 J m^{-2} ($\text{APE}_{\text{err}} = -0.2$), respectively.
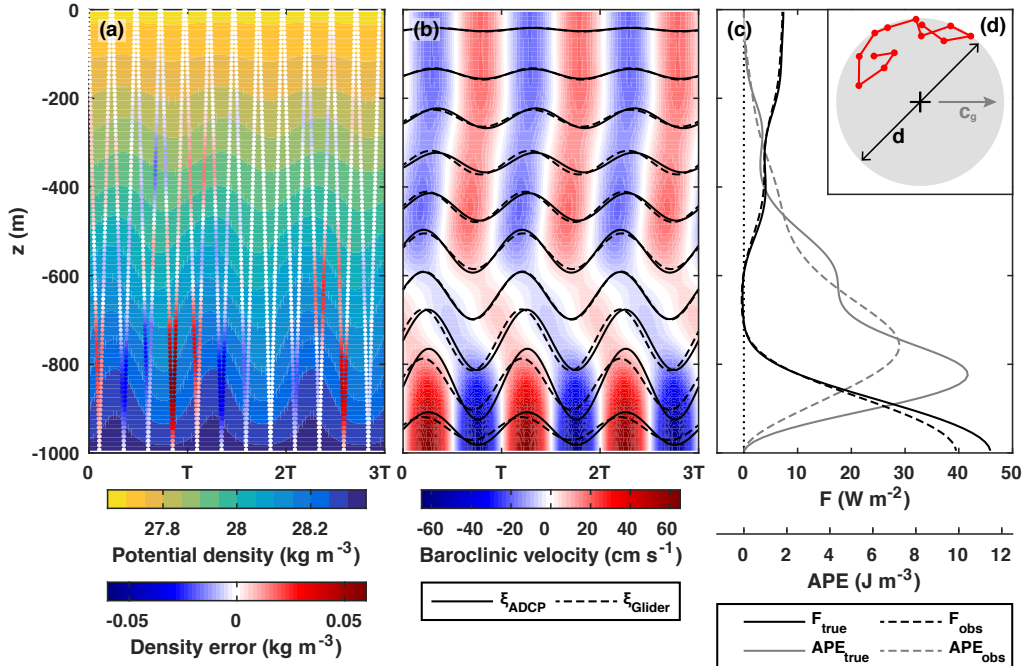
Figure 7. (a) Potential density for an idealised M_2 multi-mode internal tide overlaid with the error in measured density due to imperfect co-location of a glider and ADCP. The x-axis is time in M_2 cycles. Positive error indicates an overestimation of density. (b) Baroclinic velocity (colour) for the same idealised internal tide overlaid with vertical isopycnal displacement at the ADCP (ξ_{ADCP}, solid black lines) and calculated from measured density (ξ_{Glider}, dashed black lines) every 100 m. (c) 'True' and 'observed' internal tide energy flux (black) and available potential energy (grey). (d) Location of the pseudorandomly distributed glider path (red) relative to the ADCP (black cross). The diameter of the watch circle, d = $\lambda/4$, where $\lambda = 80$ km is the mode-1 horizontal wavelength. c_g is the direction of ~~wave~~ tide propagation.

5.2 Energy flux error

Histograms of $\mathbf{F}_{\text{err}}$ (~~0.001~~0.005-wide bins) for four watch circle diameter cases are shown in Figure 8a. The peaked distribution for the $d = 1/32\lambda$ case broadens with increasing watch circle diameter as well as becoming biased towards negative error. The negative bias results from two related mechanisms. Firstly, the amplitude of ξ_{Glider} (and therefore p'_{Glider}) is typically underestimated for large watch circles because the glider samples density with a broad range of phase shifts, causing spectral smearing and poor harmonic fits to ξ. Secondly, maximum energy flux occurs when p' and $\mathbf{u}'_{\text{bc}}$ are exactly in-phase so any error in the phase of p'_{Glider}, positive or negative, will also result in a negative bias.

$\mathbf{F}_{\text{err}}$ distributions for all ~~eight~~ nine watch circle diameter cases are shown in Figure 8c, including the ~~full range (100%),~~ 99% and 95% confidence limits ~~,~~ and the bias (median value). As watch circle diameter increases, the width of the confidence intervals increases and the bias becomes progressively more negative. For the $d = 1/32\lambda$ case, $\mathbf{F}_{\text{err}}$ is $\pm$~~0.03~~0.04 at the 99%
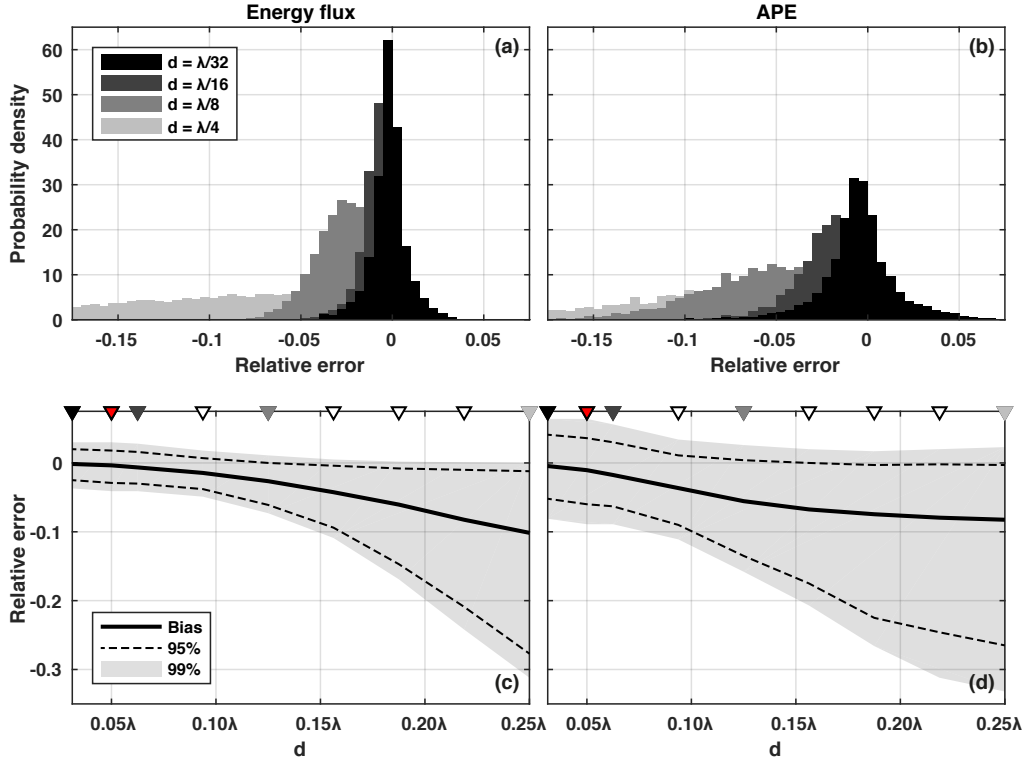
Figure 8. Histograms of (a) energy flux relative error and (b) APE relative error due to mis-sampling density in an idealised M_2 multimode internal tide field for the four watch circle diameter cases shown in Figure 6. Positive error indicates an overestimation, negative error indicates an underestimation. ~~The full range~~ Distribution of (a) ~~~~energy flux relative error and (b) ~~~~APE relative error against watch circle diameter, ~~along with~~ including the 99% and 95% confidence limits and the bias (median value). The four cases in panels (a) and (b) are indicated with black and grey triangles. The red triangle is the case most appropriate for the observations. The white triangles are four additional cases~~with intermediate watch circle diameters~~.

5   limit and the bias is near zero (−0.002). For the $d = 1/4\lambda$ case at the other extreme, $\mathbf{F}_{\mathrm{err}}$ is 0 to ~~−0.32~~ 0.31 at the 99% limit and the bias is −0.1.

5.3 APE error

Histograms of $\mathrm{APE}_{\mathrm{err}}$ for four watch circle diameter cases are shown in Figure 8b. Compared with $\mathbf{F}_{\mathrm{err}}$, the distributions are broader and with a more negative bias for small watch circles. The broader distribution is explained by the error in ξ_{Glider} being squared in Equation 9. The negative bias is explained by the first mechanism described in Section 5.2. $\mathrm{APE}_{\mathrm{err}}$ distributions for all ~~eight~~ nine watch circle diameter cases are shown in Figure 8d. Similar to $\mathbf{F}_{\mathrm{err}}$, the width of the confidence intervals increases and the bias becomes progressively more negative as watch circle diameter increases. For $d = 1/32\lambda$, $\mathrm{APE}_{\mathrm{err}}$ is ±~~0.06~~ 0.08 at the 99% limit and the bias is ~~near zero~~ only −0.005. For $d = 1/4\lambda$, $\mathrm{APE}_{\mathrm{err}}$ is 0.02 to ~~−0.34~~ 0.33 at the 99%

16

d (km)	d/λ	$\mathbf{F}_{\text{err}}$					A	
		99%	95%	Bias	95%	99%	99%	95%
2.5	0.03125	−~~0.033~~ 0.037	−~~0.023~~ 0.025	−0.002	~~0.018~~ 0.020	~~0.028~~ 0.030	−~~0.066~~ 0.081	−~~0.045~~ 0.052
4.0	**0.05**	**−0.041**	**−0.029**	**−0.004**	**0.018**	**0.030**	**−0.089**	**−0.060**
5.0	0.0625	−~~0.040~~ 0.041	−~~0.029~~ 0.030	−0.007	~~0.014~~ 0.016	~~0.027~~ 0.028	−~~0.079~~ 0.089	−~~0.061~~ 0.063
7.5	0.09375	−~~0.048~~ 0.049	−0.038	−0.015	~~0.008~~ 0.007	~~0.017~~ 0.018	−~~0.110~~ 0.111	−~~0.088~~ 0.090
10.0	0.125	−~~0.071~~ 0.073	−0.061	−0.027	~~0.001~~ 0.000	~~0.013~~ 0.011	−~~0.163~~ 0.158	−~~0.132~~ 0.135
12.5	0.15625	−~~0.118~~ 0.109	−~~0.097~~ 0.094	−~~0.044~~ 0.043	−~~0.005~~ 0.004	0.005	−~~0.222~~ 0.207	−~~0.183~~ 0.175
15.0	0.1875	−~~0.166~~ 0.169	−~~0.146~~ 0.147	−~~0.062~~ 0.061	−~~0.007~~ 0.008	~~0.003~~ 0.002	−~~0.281~~ 0.266	−~~0.214~~ 0.225
17.5	0.21875	−~~0.237~~ 0.242	−~~0.208~~ 0.209	−~~0.082~~ 0.083	−0.010	~~0.000~~ 0.001	−~~0.304~~ 0.312	−~~0.247~~ 0.246
20.0	0.25	−~~0.315~~ 0.312	−~~0.276~~ 0.277	−~~0.105~~ 0.102	−~~0.014~~ 0.012	−~~0.003~~ 0.000	−~~0.341~~ 0.332	−~~0.264~~ 0.265

Table 2. Distributions of energy flux relative error ($\mathbf{F}_{\text{err}}$) and APE relative error (APE_{err}) for all ~~eight~~ nine watch circle diameter cases. d/λ is watch circle diameter to mode-1 horizontal wavelength ratio. Positive error indicates overestimation, negative error indicates underestimation. The case most appropriate for the observations ($d/\lambda = 0.05$) is in bold.

limit and the bias is −0.08. Unlike $\mathbf{F}_{\text{err}}$, the bias converges towards a constant value ~~(approximately −0.08)~~ for very large watch circles.

6 Summary and discussion

A novel approach to measuring internal tide energy flux using a co-located ocean glider and moored ADCP is tested using a dataset collected from the WTR in the North Atlantic. Gliders cannot perfectly hold station, even when operating as a virtual mooring, so error in the energy flux calculation due to imperfect co-location of the glider and ADCP is estimated by sub-sampling potential density in an idealised internal tide field along pseudorandomly distributed glider paths. If we consider the maximum acceptable energy flux error to be 0.1 (10%), all the glider data must be contained within a watch circle with a diameter smaller than 1/8 the mode-1 horizontal wavelength of the internal tide. Energy flux is biased low and the negative bias increases with increasing watch circle diameter. If watch circle diameter is larger than 1/8 the mode-1 horizontal wavelength, the negative bias is more than −0.03 (3%) and all realisations within the 95% confidence ~~limits~~ interval are underestimates. When on-station over the WTR, the glider stayed within 2.5 km of the mooring so watch circle diameter, $d = 5$ km. The local ~~M_2~~ D_2 mode-1 horizontal wavelength, $\lambda \approx 100$ km so ~~$d/\lambda \approx 0.05$. From~~ the $d/\lambda = 0.05$ case (Table 2~~, the~~) is the most appropriate for the observations presented here. The observed energy flux is estimated to have a negative bias of only ~~−0.005 (0.5~~ −0.004 (0.4%) and an error of less than ±~~0.04 (4~~0.03 (3%) at the ~~99~~95% confidence limit. This estimate does not include the effect of internal tide advection by the barotropic tide (Stephenson et al., 2016), which can lead to an additional negative bias if barotropic velocity amplitude is of a similar size to baroclinic phase speed. Over the WTR, ~~M_2~~ D_2 mode-1 phase speed is ≈ 2.2 m s^{-1} and barotropic velocity amplitude is < 0.2 m s^{-1} so we expect this effect to be negligible for our observations.

At mid-latitudes, M_2 D_2 mode-1 horizontal wavelength for a 1000-m deep water column is typically in the range 40-160 km. The results presented here suggest energy flux error due to imperfect co-location can be reduced to an acceptable level (10%) if the glider maintains a 5-km to 20-km diameter watch circle. In the absence of strong tidal and slope currents, a well-trimmed glider diving to 1000 m with a relatively steep glide angle can usually maintain a watch circle with a diameter of 5 km or less, so energy flux error will typically be <10%. Where horizontal wavelengths are shorter, for example at lower latitudes or in shallower and less stratified water columns, a smaller watch circle will be required to maintain an acceptable level of error. In shallower water, smaller watch circles are generally achievable because horizontal travel over a complete dive cycle scales with dive depth. Diurnal internal tides have longer horizontal wavelengths so larger watch circles are acceptable. For mission planning, the mode-1 horizontal wavelength of a tidal frequency ω can be estimated $\lambda = 2\pi c_1 / \sqrt{\omega^2 - f^2}$, where f is the inertial frequency and $c_1 = NH/\pi$ is an approximation of mode-1 eigenspeed. If the assumption of uniform stratification is not appropriate, c_1 can be calculated by solving the boundary value problem for a given $N(z)$ (Gill, 1982). Table 2 can then be used to estimate the energy flux bias and error that can be expected for a given value of d/λ.

Including the above estimate of error due to imperfect co-location, the observed ~~semidiurnal~~ depth-integrated D_2 internal tide energy flux over the northern flank of the WTR is 4.2 ± 0.2 kW m^{-1}. This is considerably larger than previous internal tide observations over the southeastern bank of the FSC: 0.2 kW m^{-1} (90 km northeast of the WTR; Hall et al., 2011) and 0.4-0.6 kW m^{-1} ~~(105 km; Hall et al., 2017b)~~(105 km northeast of the WTR; Hall et al., 2017b), but small compared with some deep-ocean ridges, for example the Hawaiian Ridge (up to 33 kW m^{-1}; Lee et al., 2006) and Luzon Strait (up to 41 kW m^{-1}; Alford et al., 2011). More comparable to the WTR is the Mendocino Escarpment, where a ridge is orientated perpendicular to the continental slope and the observed energy flux is 7 kW m^{-1} (Althaus et al., 2003).

The 40-hour co-located timeseries presented here is not long enough to resolve the internal spring-neap cycle~~and therefore all M_2 harmonic fits are contaminated with S_2 variability~~. Peak neap tide occurred on yearday 153, one day before the majority of the co-located timeseries. Assuming the internal tide is generated locally at the WTR, the surface and internal spring-neap cycles will be in phase. The observed ~~semidiurnal~~ D_2 energy flux is therefore representative of neap internal tide and so an underestimate of the true M_2 internal tide. This may somewhat explain the slight underestimate compared to the M_2-only regional tide model. Interestingly, the CTD timeseries used by Sherwin (1991) was recorded two days after peak spring tide so is more representative of spring internal tide. The fact that two observational estimates of ~~semidiurnal~~ D_2 vertical isopycnal displacement, 6.7 km apart and at different phases of the internal spring-neap cycle, are so similar, implies that there are compensating spatial gradients in internal tide magnitude. The regional tide model shows the possible extent of these gradients and suggests that accurate siting of moorings is crucial for repeated, long-term observations.

For future experiments, spatial gaps in the timeseries can be minimised with conductivity-temperature loggers and additional current meters on the mooring line. We have also shown that glider-inferred DAC can provide an accurate estimate of tidal current velocity that could be used to constrain barotropic velocity in the absence of full-depth data coverage by ADCPs and current meters. However, the major limitation of the dataset presented here is the short length of the co-located timeseries. Future glider missions will hold station ~~over~~ by an ADCP mooring for several weeks to resolve the internal spring-neap cycle. Calculating ~~semidiurnal~~ D_2 internal tide energetics in a 36-hour moving window will yield a time-varying energy flux that can

5 be related to seasonal changes in stratification, advection by mesoscale eddies, spatial and temporal patterns ~~baroclinic shear instabilities, turbulent mixingrates, and biogeochemical responses~~ in internal tide-driven turbulent mixing, and the resulting biogeochemical response.

Appendix A: Idealised internal tide field

An idealised M_2 multi-mode internal tide field is created for a 1000-m deep ~~watercolumn~~ water column with uniform stratification ($N^2 = 6.1 \times 10^{-6}$ s^{-2}). Horizontal current velocity, $\mathbf{u} = (u, v)$, and vertical isopycnal displacement, ξ, are defined by summing the first ten baroclinic modes,

$$15 \quad u(x, y, z, t) = \sum_{n=1}^{10} u_n \sin(k_n x - \omega t - \phi_n) A_n(z), \tag{A1}$$

$$v(x, y, z, t) = \sum_{n=1}^{10} u_n \frac{f}{\omega} \cos(k_n x - \omega t - \phi_n) A_n(z), \text{ and} \tag{A2}$$

$$\xi(x, y, z, t) = \sum_{n=1}^{10} u_n \sin(k_n x - \omega t - \phi_n) B_n(z) \frac{1}{\omega} \left(\frac{\omega^2 - f^2}{N^2 - \omega^2} \right)^{1/2}, \tag{A3}$$

20 where u_n and ϕ_n are the velocity amplitude and the phase of the n-th baroclinic mode, respectively, $\omega = 1.41 \times 10^{-4}$ s^{-1} is the M_2 frequency, and $f = 1.26 \times 10^{-4}$ s^{-1} is the inertial frequency at 60°N. $A_n(z)$ and $B_n(z)$ are the vertical structures of horizontal current velocity and vertical isopycnal displacement for each baroclinic mode, and are equivalent to $\cos(n\pi z/H)$ and $\sin(n\pi z/H)$, respectively, where n is mode number. Horizontal wavenumber, $k_n = \sqrt{\omega^2 - f^2}/c_n$, where $c_n = NH/n\pi$ is an approximation of mode eigenspeed (Gill, 1982). Velocity amplitude decays with mode number, $u_n = u_1 e^{-0.5(n-1)}$,
25 where u_1 is the mode-1 velocity amplitude. This decay rate results in a well-defined internal tide beam if velocity phase is approximately equal for each baroclinic mode. However, a different random set of baroclinic mode phases (ϕ_n) is used for each scenario simulated so internal tide beams are only apparent in a subset of scenarios. $u_1 = 0.28$ m s^{-1} ~~is the mode-1 velocity amplitude and~~ yields a mode-1 vertical isopycnal displacement amplitude of 50 m~~. Energy~~, but energy flux error and APE error are not sensitive to ~~mode-1 velocity~~ absolute amplitude. The time-varying potential density field is then

$$5 \quad \rho(x, y, z, t) = \overline{\rho}(z) + \frac{\rho_0}{g} N^2 \xi, \tag{A4}$$

19

where $\overline{\rho}(z)$ is a background density profile with a vertical gradient equivalent to N^2. Barotropic velocity ($\mathbf{u}'_{\mathrm{bt}}$) and residual flow ($\overline{\mathbf{u}}$) are both zero so $\mathbf{u}'_{\mathrm{bc}} = \mathbf{u}$. ~~A different set of random baroclinic mode phases (ϕ_n) are used for each scenario simulated.~~

References

Alford, M. H., MacKinnon, J. A., Nash, J. D., Simmons, H., Pickering, A., Klymak, J. M., Pinkel, R., Sun, O., Rainville, L., Musgrave, R., Beitzel, T., Fu, K.-H., and Lu, C.-W.: Energy flux and dissipation in Luzon Strait: Two tales of two ridges, Journal of Physical Oceanography, 41, 2211–2222, doi:10.1175/JPO–D–11–073.1, 2011.

10   Althaus, A. M., Kunze, E., and Sanford, T. B.: Internal tide radiation from Mendocino Escarpment, Journal of Physical Oceanography, 33, 1510–1527, 2003.

Baines, P. G.: On internal tide generation models, Deep-Sea Research, 29, 307–338, 1982.

Blumberg, A. F. and Mellor, G. L.: A description of a three-dimensional coastal ocean circulation model, in: Three-Dimensional Coastal Ocean Models, Vol. 4, edited by Heaps, N. S., pp. 1–16, American Geophysical Union, Washington, DC, 1987.

15   Boettger, D., Robertson, R., and Rainville, L.: Characterizing the semidiurnal internal tide off Tasmania using glider data, Journal of Geophysical Research: Oceans, 120, 3730–3746, doi: 10.1002/2015JC010 711, 2015.

Emery, W. J. and Thomson, R. E.: Data Analysis Methods in Physical Oceanography, Elsevier, Amsterdam, second edn., 2001.

Eriksen, C. C., Osse, T. J., Light, R. D., Wen, T., Lehman, T. W., Sabin, P. J., Ballard, J. W., and Chiodi, A. M.: Seaglider: a long-range autonomous underwater vehicle for oceanographic research, IEEE Journal of Oceanic Engineering, 26, 424–436, doi:10.1109/48.972 073,

20   2001.

Frajka-Williams, E., Eriksen, C. C., Rhines, P. B., and Harcourt, R. R.: Determining vertical water velocities from Seaglider, Journal of Atmospheric and Oceanic Technology, 28, 1641–1656, doi:10.1175/2011JTECHO830.1, 2011.

Garau, B., Ruiz, S., Zhang, W. G., Pascual, A., Heslop, E., Kerfoot, J., and Tintoré, J.: Thermal lag correction on Slocum CTD glider data, Journal of Atmospheric and Oceanic Technology, 28, 1065–1071, doi:10.1175/JTECH–D–10–05 030.1, 2011.

25   Gill, A. E.: Atmosphere-Ocean Dynamics, Academic Press, 1982.

Hall, R. A., Huthnance, J. M., and Williams, R. G.: Internal tides, nonlinear internal wave trains, and mixing in the Faroe-Shetland Channel, Journal of Geophysical Research, 116, C03 008, doi:10.1029/2010JC006 213, 2011.

Hall, R. A., Aslam, T., and Huvenne, V. A. I.: Partly standing internal tides in a dendritic submarine canyon observed by an ocean glider, Deep-Sea Research Part I, 126, 73–84, doi:10.1016/j.dsr.2017.05.015, 2017a.

30   Hall, R. A., Berx, B., and Inall, M. E.: Observing internal tides in high-risk regions using co-located ocean gliders and moored ADCPs, Oceanography, 30, 51–52, doi:10.5670/oceanog.2017.220, 2017b.

Hopkins, J. E., Stephenson, G. R., Green, J. A. M., Inall, M. E., and Palmer, M. R.: Storms modify baroclinic energy fluxes in a seasonally stratified shelf sea: Inertial-tidal interaction, Journal of Geophysical Research: Oceans, 119, 6863–6883, doi:10.1002/2014JC010 011, 2014.

35   IOC, SCOR, and IAPSO: The international thermodynamic equation of seawater - 2010: Calculation and use of thermodynamics properties, in: Intergovernmental Oceanographic Commission, Manuals and Guides, 56, p. 196, UNESCO, 2010.

Johnston, T. M. S. and Rudnick, D. L.: Trapped diurnal internal tides, propagating semidiurnal internal tides, and mixing estimates in the California Current System from sustained glider observations, 2006-2012, Deep-Sea Research II, 112, 61–78, doi:10.1016/j.dsr2.2014.03.009, 2015.

Johnston, T. M. S., Rudnick, D. L., Alford, M. H., Pickering, A., and Simmons, H. J.: Internal tide energy fluxes in the South China Sea from

5   density and velocity measurements by gliders, Journal of Geophysical Research: Oceans, 118, 3939–3949, doi:10.1002/jgrc.20 311, 2013.

Johnston, T. M. S., Rudnick, D. L., and Kelly, S. M.: Standing internal tides in the Tasman Sea observed by gliders, Journal of Physical Oceanography, 45, 2715–2737, doi:10.1175/JPO–D–15–0038.1, 2015.

Kunze, E., Rosenfeld, L. K., Carter, G. S., and Gregg, M. C.: Internal waves in Monterey Submarine Canyon, Journal of Physical Oceanography, 32, 1890–1913, 2002.

10 Lee, C. M., Kunze, E., Sanford, T. B., Nash, J. D., Merrifield, M. A., and Holloway, P. E.: Internal tides and turbulence along the 3000-m isobath of the Hawaiian Ridge, Journal of Physical Oceanography, 36, 1165–1182, 2006.

Nash, J. D., Alford, M. H., and Kunze, E.: Estimating internal wave energy fluxes in the ocean, Journal of Atmospheric and Oceanic Technology, 22, 1551–1570, 2005.

Pingree, R. D., Mardell, G. T., and New, A. L.: Propagation of internal tides from the upper slopes of the Bay of Biscay, Nature, 321,

15   154–158, 1986.

Queste, B. Y.: Hydrographic observations of oxygen and related physical variables in the North Sea and Western Ross Sea Polynya, Ph.D. thesis, School of Environmental Sciences, University of East Anglia, 2014.

Rainville, L., Lee, C. M., Rudnick, D. L., and Yang, K.-C.: Propagation of internal tides generated near Luzon Strait: Observations from autonomous gliders, Journal of Geophysical Research, 118, 4125–4138, doi:10.1002/jgrc.20 293, 2013.

20 Rudnick, D. L. and Cole, S. T.: On sampling the ocean using underwater gliders, Journal of Geophysical Research, 116, C08 010, doi:10.1029/2010JC006 849., 2011.

Rudnick, D. L., Johnston, T. M. S., and Sherman, J. T.: High-frequency internal waves near the Luzion Strait observed by underwater gliders, Journal of Geophysical Research, 118, 1–11, doi:10.1002/jgrc.20 083, 2013.

Sharples, J., Tweddle, J. F., Green, J. A. M., Palmer, M. R., Kim, Y.-N., Hickman, A. E., Holligan, P. M., Moore, C. M., Rippeth, T. P.,

25   Simpson, J. H., and Krivtsov, V.: Spring-neap modulation of internal tide mixing and vertical nitrate fluxes at a shelf edge, Limnology and Oceanography, 52, 1735–1747, 2007.

Sharples, J., Ellis, J. R., Nolan, G., and Scott, B. E.: Fishing and the oceanography of stratified shelf seas, Progress in Oceanography, 117, 130–139, doi:10.1016/j.pocean.2013.06.014, 2013.

Sherwin, T. J.: Evidence of a deep internal tide in the Faeroe-Shetland channel, in: Tidal Hydrodynamics, edited by Parker, B. B., pp.

30   469–488, John Wiley & Sons, New York, 1991.

Stephenson, G. R., Green, J. A. M., and Inall, M. E.: Systematic bias in baroclinic energy estimates in shelf seas, Journal of Physical Oceanography, 46, 2851–2862, doi:10.1175/JPO–D–15–0215.1, 2016.

Todd, R. E., Rudnick, D. L., Sherman, J. T., Owens, W. B., and George, L.: Absolute velocity estimates from autonomous underwater gliders equipped with Doppler current profilers, Journal of Atmospheric and Oceanic Technology, 34, 309–333, doi:10.1175/JTECH–D–16–

435   0156.1, 2017.

Zhao, Z., Alford, M. H., Lien, R.-C., Gregg, M. C., and Carter, G. S.: Internal tides and mixing in a submarine canyon with time-varying stratification, Journal of Physical Oceanography, 42, 2121–2142, doi:10.1175/JPO–D–12–045.1, 2012.